From Dry to Wet Vertex Model Dynamics

Rozman, Jan; Kanala Venkata, Sravana Chaithanya; Yeomans, Julia; Sknepnek, Rastko

Publication date:
2023

Document Version
Early version, also known as pre-print

From Dry to Wet Vertex Model Dynamics: Generating Sustained Flows

Jan Rozman,[1,*] Chaithanya K. V. S.,[2,*] Julia M. Yeomans,[1,†] and Rastko Sknepnek[2,3,‡]

[1] *Rudolf Peierls Centre for Theoretical Physics, University of Oxford, Oxford OX1 3PU, United Kingdom*
[2] *School of Science and Engineering, University of Dundee, Dundee DD1 4HN, United Kingdom*
[3] *School of Life Sciences, University of Dundee, Dundee DD1 5EH, United Kingdom*

(Dated: December 20, 2023)

Complex tissue flows in epithelia are driven by intra- and inter-cellular processes that generate, maintain, and coordinate mechanical forces. There has been growing evidence that cell shape anisotropy, manifested as nematic order, plays an important role in this process. Here we extend a nematic vertex model by replacing substrate friction with internal viscous dissipation, of relevance to epithelia not supported by a substrate or the extracellular matrix, such as many early-stage embryos. When coupled to cell shape anisotropy, the internal viscous dissipation allows for long-range velocity correlations and thus enables the spontaneous emergence of flows with a large degree of spatiotemporal organisation. We demonstrate sustained flow in epithelial sheets confined to a channel, thus providing a link between the dynamical behaviour of continuum active nematics and the cell-level vertex model of tissue dynamics.

Introduction.—Collective cell migration, i.e., a coordinated movement of groups of cells that maintain contacts and coordinate intercellular signalling, [1, 2] underlies wound healing [3, 4], cancer invasion [5, 6], and embryonic development [7, 8]. Proper execution of these biological processes necessitates the generation and robust spatiotemporal regulation of large-scale coordinated flows [9]. How such tissue-scale flows emerge from coordination between molecular processes and cell-level behaviours such as cell intercalation, division, and ingression is poorly understood.

In vitro experiments on epithelial cell monolayers grown on soft substrates [10–13] reveal that collective cell migration is an emergent active phenomenon that requires maintenance, transmission and coordination of mechanical forces over distances large compared to the cell size. Dense cell packing and fluctuations driven by active cellular processes lead to correlated patterns in cell displacements [14, 15] reminiscent of the glass transition between liquid and solid phase. This transition is related to cell shape [16–18] and cell-cell adhesion [19], allowing epithelia to control their rheological properties.

Theories of the physics of active matter [20–23] have been instrumental in understanding many aspects of the collective behaviour in epithelial cell monolayers [24–26]. Two key components in migration on substrates are active contractile forces that cells exert on the substrate and planar cell polarity [27]. Together, they enable directional cell motion. Models of self-propelled dense active matter are, therefore, able to capture many aspects of collective cell behaviours. While such models come in many guises [28], e.g., particle-based approaches, phase-field methods, cellular Potts models, Voronoi models, and vertex models, in almost all cases dissipation is modelled as being proportional to the local cell velocity. Due to momentum exchange with the substrate, the momentum of the cell layer is not conserved and the system is referred to as being in the *dry* limit. [20] This is an appropriate assumption for cells adhered to a substrate.

On the other hand, e.g. during gastrulation in avian embryos, an extracellular matrix is not yet fully formed and cells in the epiblast are not supported by a substrate [29]. Cell movements can, therefore, only result from forces that cells exert onto each other, which can be modelled as active feedback between tension and the density of molecular motors [30–35] or cell shape and tension [36, 37]. Because there is no friction with the substrate dissipation needs to be internal, i.e. due to the cells moving past each other. Here we use the vertex model with active anisotropic stress coupled to local cell elongation [36, 38] and internal viscous dissipation proportional to the vertex velocity relative to velocities of its neighbours [39] to study active flows in tissues not supported by a substrate. This corresponds to the *wet* limit in active matter.

Using a narrow channel geometry, we show that, unlike in the dry case, the wet active vertex model can develop spontaneous directional flows due to long-range velocity-velocity correlations. This model, therefore, provides the plausible necessary ingredients for a cell-level description of large-scale active flows in epithelia not supported by a substrate. It also outlines a possible connection between cell-level and continuum descriptions based on theories of active nematics [40], that are able to capture morphogenic flows [41, 42], but where the activity is introduced phenomenologically. In addition to being relevant for modelling early development, geometric constraints have been shown to impact collective cell migration, e.g., by a width-driven transition from a state of no net flow to shear flow in the elongated retinal pigment epithelial cells and mouse myoblasts [43], or geometry-controlled global and multinodal oscillations in Madin-Darby canine kidney (MDCK) cells [44, 45].

Model.—We study the vertex model in its canonical

* These authors contributed equally to this work.
† julia.yeomans@physics.ox.ac.uk
‡ r.sknepnek@dundee.ac.uk

form [46] in which the energy function reads

$$E_{\rm VM} = \sum_c \left[\frac{K_A}{2} \left(A_c - A_0\right)^2 + \frac{K_P}{2} \left(P_c - P_0\right)^2 \right], \quad (1)$$

where the sum is over all cells. K_A and K_P are, respectively, the area and perimeter elasticity moduli, A_c and P_c are the area and perimeter of cell c, whereas A_0 and P_0 are the target area and perimeter, taken to be the same for all cells. The usual approach assumes overdamped dynamics with dissipation modelled as the vertex-substrate frictional force $-\eta \mathbf{v}_i$, where η is the friction coefficient and $\mathbf{v}_i$ is the velocity of vertex i. This is, however, not appropriate for suspended epithelia and an alternative model for dissipation is necessary, e.g., as recently proposed in Ref. 39. The dissipative force on vertex i is instead dominated by contributions arising from the difference between its velocity and the velocities of its neighbours (Fig. 1). The equation of motion thus becomes

$$\eta \dot{\mathbf{r}}_i + \xi \sum_{j \in \mathcal{S}_i} \left(\dot{\mathbf{r}}_i - \dot{\mathbf{r}}_j\right) = -\nabla_{\mathbf{r}_i} E_{\rm VM} + \mathbf{f}_i^{\rm act}, \quad (2)$$

where ξ is the vertex-vertex friction coefficient and the sum is over vertices j in the star $\mathcal{S}_i$ of (i.e., connected to) the vertex i. $E_{\rm VM}$ is the elastic energy, $\nabla_{\mathbf{r}_i}$ is the gradient with respect to the position vector $\mathbf{r}_i$ of vertex i, and $\mathbf{f}_i^{\rm act}$ is the active force on vertex i. In the limit, $\xi \to 0$, Eq. (2) reduces to the familiar overdamped equation of motion.

The active force on vertex i arises from cell-level stresses due to cell elongation [36]. It is given as $\mathbf{f}_{\rm act}^i = -\tilde{\mathbf{r}}_i \cdot \boldsymbol{\sigma}_c$, where $\boldsymbol{\sigma}_c = -\zeta \mathbf{Q}_c$ is the stress tensor [47] and $\tilde{\mathbf{r}}_i = \frac{1}{2}(\mathbf{r}_{i+1} - \mathbf{r}_{i-1}) \times \hat{\mathbf{z}}$, with $\mathbf{r}_{i+1}$ and $\mathbf{r}_{i-1}$ being respectively the vertices following and preceding i in counterclockwise order around cell c [38, 48]. ζ measures strength of activity and $\mathbf{Q}_c = \frac{1}{P_c} \sum_j \ell_j \hat{\mathbf{t}}_j \otimes \hat{\mathbf{t}}_j - \frac{1}{2}\mathbf{I}$. Here, the sum is over all junctions j of cell c, ℓ_j is the length of the $j^{\rm th}$ junction, $\mathbf{t}_j$ is a unit-length vector along said junction, and $\mathbf{I}$ is the identity tensor. For sufficiently high positive values of ζ, this model with dry dynamics generates active chaotic flows reminiscent of extensile active nematics in terms of, e.g., the velocity profiles around $\pm 1/2$ topological defects [36]. Here we, therefore, focus on the $\zeta > 0$ (i.e., extensile) case. See Methods for details of model implementation.

We choose $A_0 = 1$, $K_A = 1$, and $\xi = 1$ ($\eta = 1$) for the wet (dry) model. This sets the units of length as $\sqrt{A_0}$, time as $\xi/(K_A A_0)$ (or $\eta/(K_A A_0)$ for the dry model), energy as $K_A A_0^2$, stress as $K_A A_0$, and the shape parameter $p_0 = P_0/\sqrt{A_0} \equiv P_0$. In these units, $E_{\rm VM} = (1/2)\sum_c \left[\left(A_c - 1\right)^2 + K_P \left(P_c - p_0\right)^2\right]$. In the wet case, $\eta/\xi = 10^{-5}$, and, unless stated otherwise, $K_P = 0.02$ and $p_0 = 3.85$.

Drawing analogies with continuum models of active nematics, which have a defined sequence of transitions when confined to a channel [49], we are interested in how these compare with active nematic vertex models under similar confinement. To create a channel, vertices of cells in the outermost top and bottom layers were affixed to a line, representing no-slip boundary conditions. As cells on the channel wall have their spacing set by the starting hexagonal lattice, but the extensile activity results in cell elongation, they tilt at an angle to the wall. Boundary conditions along the other dimension are periodic. See Methods for details of channel implementation.

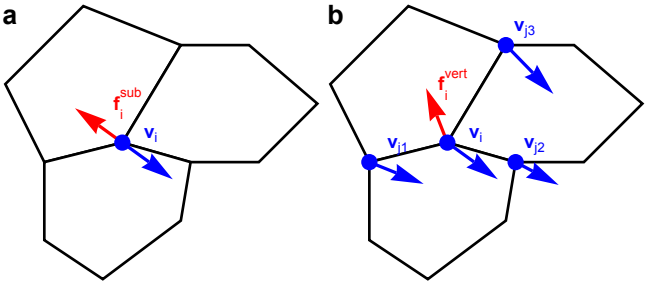

FIG. 1. **Schematic of different friction models**. **a**) In the dry model, each vertex experiences a frictional force due to the substrate. This force points in the exactly opposite direction to the vertex velocity. **b**) In the wet model, friction on a vertex is due to its motion relative to the other vertices it is connected to, and the direction of the friction force therefore also depends on the velocity of those vertices.

Results.—We first simulated a channel of width $N_y = 14$ cells using the dry model with activity $\zeta = 0.01 - 0.2$. We found no evidence of channel-wide unidirectional flows for any activity (Fig. 2a,c and Movie S1). By contrast, the wet model developed clear unidirectional flows for sufficiently high activities (Fig. 2b,d and Movie S2). To quantify flows, we measured the mean-squared displacement of cells after flows emerged, confirming that the cell movement is ballistic in the wet, but not in the dry model (Fig. 2e, Extended Data Fig. 3 and Methods). Moreover, the mean velocity for a given activity decreases sharply with increasing friction (Fig. 2f). The dry model for studied channel widths between $N_y = 6$ and 20 cannot sustain unidirectional channel flows. This remains true even if the simulation starts with wet dynamics so that a flow profile emerges, and it is then changed to being dry (Extended Data Figure 3 and Methods).

In Fig. 3a, we plot how the mean cell velocity along the channel (Methods) depends on the activity and the channel width showing that both higher activities and wider channels lead to higher mean velocities. In Fig. 3b we plot the velocity profiles in the wet channel as a function of the activity for $N_y = 14$. For sufficiently high ζ the cell velocities reach a maximum in the centre of the channel and decrease towards the walls as in the continuum theories [40].

For a narrow range of activities just above the critical value required for flows (up to ~ 0.02 above the threshold value), the flow profile across the channel in the vertex model crosses over to that of plug flow, uniform, except close to the boundaries (inset of Fig. 3b). This behaviour differs from that in continuum theories

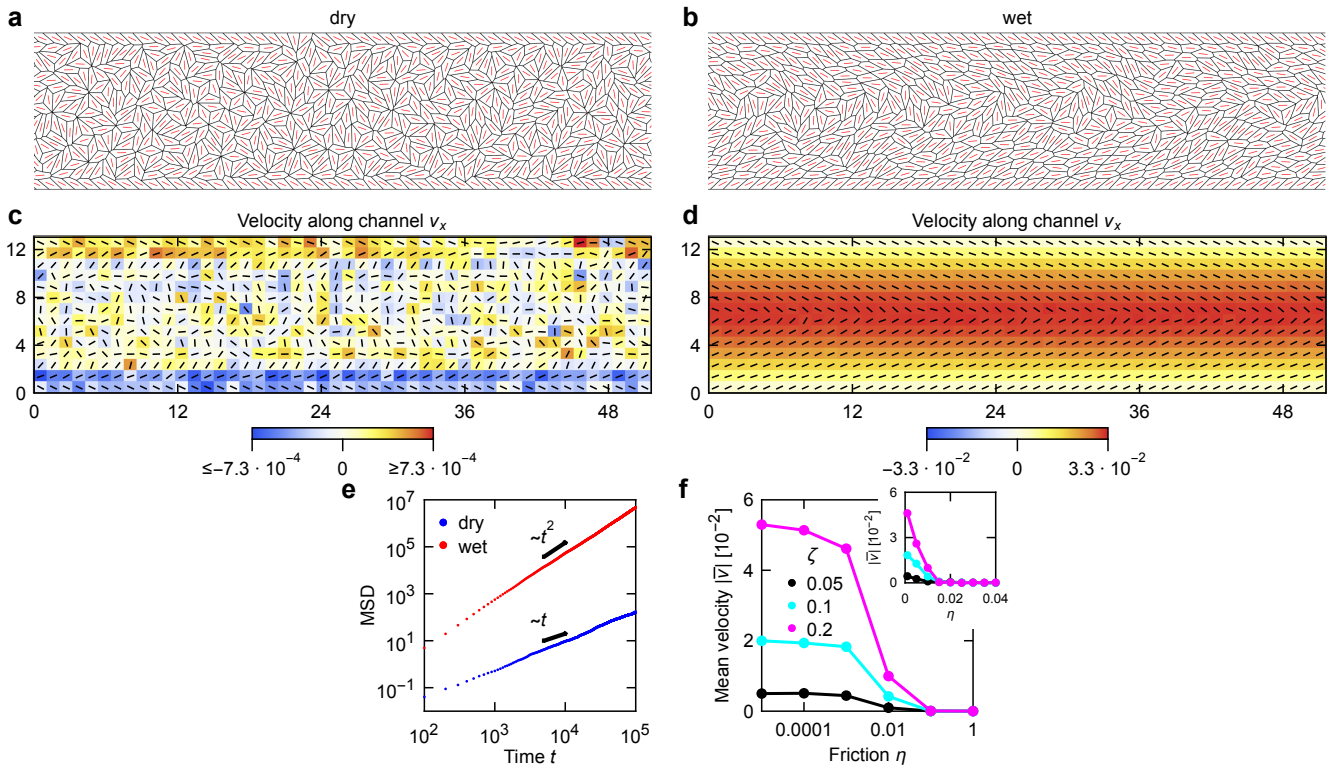

FIG. 2. **Comparison of dry and wet model dynamics in a channel**. **a**&**b**) Model tissue at $t = 2 \cdot 10^5$ for a dry (**a**) and wet (**b**) model at $\zeta = 0.1$ and size $N_x = 48$ by $N_y = 14$ cells. Cell directors are shown in red. **c**&**d**) The corresponding cell velocity profiles along x for the dry (**c**) and wet (**d**) models, averaged between $t = 1 \cdot 10^5$ and $t = 2 \cdot 10^5$ in increments of $\Delta t = 500$, overlaid with the averaged director profiles (black lines). **e**) Mean-squared displacement as a function of time for the dry and wet model tissues from panels **a** and **b**, respectively. The best power-law fit exponents are 1.1 (dry) and 2.0 (wet). **f**) Mean velocity as a function of substrate friction for different activities. Inset focuses on the transition in linear scale. Data for $N_y = 14$. Points on panel **f** are connected for clarity.

and is a consequence of the rhombile state that emerges in the model [36]. At the lowest activities that allow for sustained flows, while the model cells inside the channel flow relative to the no-slip cells at the channel wall, the bulk cells jam and move very little relative to each other (Fig. 3c and Movie S3).

To investigate this further, we determined how the threshold activities ζ_c for the onset of unidirectional flows depend on activity and channel width, by performing simulations that initially started at a higher activity ($\zeta = 0.1$ for $p_0 > 3.8$, $\zeta = 0.2$ for $p_0 \leq 3.8$) until time $t = 10^5$ so that flows develop. After that, we instantaneously reduced the activity to the final value and continued the simulation until time $t = 3 \cdot 10^5$ (inset of Fig. 3a). Interestingly, the threshold activity does not depend strongly on the channel width, by comparison to the continuum theories where it is proportional to the inverse of squared channel width [40]. This can be explained by noting that in the jammed state there is no motion of cells relative to each other (i.e., no dissipation), so a force of fixed magnitude is sufficient to cause an arbitrarily wide tissue to flow. The threshold activity does depend on the target perimeter p_0, with higher p_0 corresponding to lower ζ_c. This is likely because the energy cost for T1 transitions decreases (and eventually vanishes) with increasing p_0, at least in the passive model. However, the threshold activity does not decay to 0 for the entire studied range of target perimeters, up to $p_0 = 4$ (Extended Data Fig. 2).

The ability of the wet model to form correlated channel-wide flows suggests the existence of long-range correlations. To investigate this further, we defined the velocity-velocity correlation function

$$C_{\mathbf{v}}(R) = \frac{\langle \mathbf{v}_c \cdot \mathbf{v}_{c'} \rangle_{R_{c,c'} \approx R}}{\langle \mathbf{v}_c \cdot \mathbf{v}_c \rangle_c} \tag{3}$$

where v_c is the velocity of cell c. The average in the numerator is over all pairs of cells c and c' whose centres are in the range $(R - \Delta R, R]$ (using the minimum-image convention [50]) and setting $\Delta R = 1$. The average in the denominator is over all cells in the tissue, hence, $C_{\mathbf{v}}(0) = 1$. Similarly, the director-director correlation function is

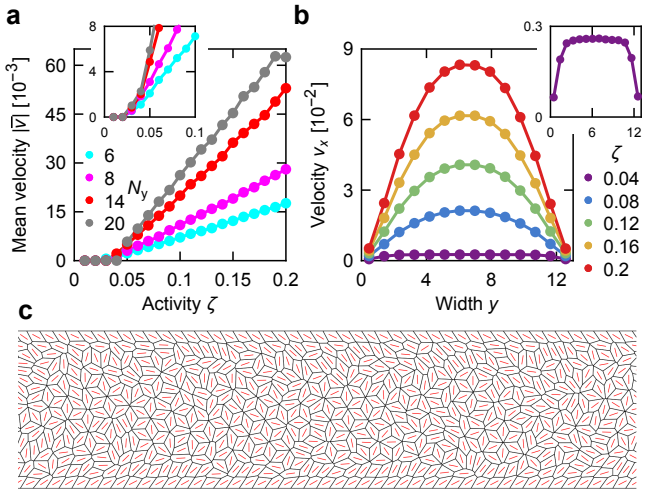

FIG. 3. **Flows in a channel**. **a**) Mean velocity as a function of activity for different channel widths in a wet model. The inset shows the region near the threshold for simulations starting from a flow profile (Methods). **b**) Velocity profile across the channel width for different activities. The inset shows the $\zeta = 0.04$ profile. **c**) Model tissue with $p_0 = 3.85$, $\zeta = 0.04$ at $t = 2 \cdot 10^5$. All panels for $N_y = 14$.

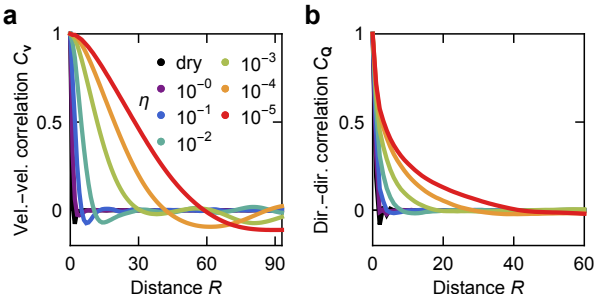

FIG. 4. **Wet dynamics allow for longer-range correlations in the vertex model**. **a**&**b**) Velocity-velocity (**a**) and director-director (**b**) correlation functions at $\zeta = 0.1$ for different values of the vertex-substrate friction η at $\xi = 1$, as well as for the dry model ($\eta = 1$, $\xi = 0$). Both panels are for a periodic model tissue with $4 \cdot 10^4$ cells at $t = 2 \cdot 10^4$.

given by

$$C_{\mathbf{Q}}(R) = \frac{\langle \mathbf{Q}_c : \mathbf{Q}_{c'} \rangle_{R_{c,c'} \approx R}}{\langle \mathbf{Q}_c : \mathbf{Q}_c \rangle_c} \tag{4}$$

where $\mathbf{Q}_c$ is the tensor used in determining the active force, and : indicates full contraction.

The correlation functions for a model with periodic boundary conditions are plotted in Fig. 4 for varying values of the surface-vertex friction η. For the dry model, ($\eta = 1$ and $\xi = 0$), both correlation functions only have a range of $\sim$ 1 cell. With decreasing η while setting $\xi = 1$, however, the correlation lengths very quickly become significantly longer, reaching $\sim$ 30 cell lengths for $\eta = 10^{-5}$ for the velocity-velocity correlation. Indeed the long correlations necessitate system sizes and simulation times that are in general computationally too costly to study with the vertex model. Specifically, a system with $4 \cdot 10^4$ cells was simulated until $t = 2 \cdot 10^4$ (compared to typically studied systems sizes of $\sim 10^3$ cells and times of $\sim 10^3$). While these simulations are sufficient to establish that in the wet model, correlations are far longer than in the dry case, it is possible that the correlations shown in Fig. 4 for the lower η values have not yet fully developed and may have been affected by the finite size of the simulation box.

Discussion and Summary.—A biologically relevant realisation of a channel would be a differentiated stripe of active cells embedded in otherwise passive tissue that would, e.g., mimic the region of an embryo that is involved in convergent extension [51]. Extended Data Fig. 4 and Movie S4 show such an example, with a stripe of softer extensile cells ($p_0 = 3.85$, $\zeta = 0.1$) surrounded by a solid passive tissue ($p_0 = 1$, $\zeta = 0$), with periodic boundary conditions. Again using the wet model, we found that the differentiated cells start to flow along the stripe. As the system is wet and periodic, the passive bulk cells are pushed in the opposite direction. Given that an external tissue presents a rheologically more complex boundary than a simple wall, it would be interesting to analyze our model in the context of viscoelastic confinement [52].

This study shows that the standard vertex model with friction with the substrate does not reproduce the channel-wide, unidirectional flows arising from nematic activity. Akin to active nematics confined to a channel, a wet model with vertex-vertex friction does however produce such flows for all studied channel widths. Moreover, wet dynamics allows a non-confined model tissue to develop long-range correlations in velocity and nematic order, whereas correlations in the dry model are limited to only the scale of a single cell. A recent study using phase-field models similarly observed longer-range correlations arising as a result of cell-cell friction [53]. Unidirectional channel flows have also been reported due to polar forces [54–57] and chiral tension modulations [58, 59].

The results highlight the importance of different modes of dissipation for collective active cell migration. Moreover, they show that the standard approach to vertex model dynamics based on substrate friction may be insufficient to explain crucial processes during embryonic development in which long-range flows emerge, e.g., as during the formation of the primitive streak in the chicken embryo [29]. This is especially important in some early stage embryos where cells are not supported by a substrate. Moreover, studying active nematic vertex models in confinement offers a way to better relate them to the well-analysed continuum active nematics, as the latter have a defined sequence of transitions in a channel [49]. As vertex models are one of the most common mechanical models of epithelia, and nematic order and activity have recently been shown to play an important role in that type of tissue [13, 60, 61], a better understanding of

how to connect this cell level approach to the extensive literature on continuum active nematic models is crucial.

METHODS

Channel model.—We studied a channel of length $N_x = 48$ cells starting with a hexagonal initial condition, with all cells having their initial areas set to A_0. Before starting the simulation, all non-affixed vertices were perturbed in a random direction by a displacement with magnitude drawn from the uniform distribution $[0, 0.1]$ so that cells had a starting elongation.

In simulations, we used a time-step $\Delta t = 0.01$. If a junction length fell below 0.01, a T1 transition was performed, and the length of the new junction was set to 0.011. Vertices on the channel wall were not allowed to move as a proxy for no-slip boundary conditions, and T1 transitions were forbidden on junctions that had a vertex on the wall.

Solving the Equations of Motion.— Since x and y directions are decoupled, Eq. (2) can be rewritten as [39]

$$\mathbf{M}\dot{\mathbf{r}}_\gamma = \mathbf{f}_\gamma. \tag{5}$$

For a system with N vertices, $\dot{\mathbf{r}}_\gamma$ and $\mathbf{f}_\gamma$ are $N-$dimensional vectors with components of, respectively, the velocity of and the force on each vertex along $\gamma \in \{x, y\}$, and $\mathbf{M}$ is an $N \times N$ sparse matrix. Assuming that each vertex is connected to three neighbours, the non-zero matrix elements are, $M_{ii} = \eta + 3\xi$ and $M_{ij} = -\xi$ for $i \neq j$ if vertices i and j share an edge. For a fixed vertex k, $M_{kj} = \delta_{kj}$ and $f_{\gamma,k} = 0$. Using $\dot{\mathbf{r}}_\gamma \approx [\mathbf{r}_\gamma(t+\Delta t) - \mathbf{r}_\gamma(t)]/\Delta t$ and rearranging terms gives

$$\mathbf{M}\ \mathbf{r}_\gamma(t+\Delta t) = \mathbf{M}\ \mathbf{r}_\gamma(t) + \Delta t \mathbf{f}_\gamma \tag{6}$$

or

$$\mathbf{r}_\gamma(t+\Delta t) = \mathbf{r}_\gamma(t) + \Delta t \mathbf{M}^{-1}\mathbf{f}_\gamma. \tag{7}$$

For periodic boundary conditions, $\mathbf{M}$ is singular for $\eta = 0$, and η was set to at least 10^{-5} in all simulations (including those of channels). Numerically, rather than computing the matrix inverse $\mathbf{M}^{-1}$, it is more efficient to solve Eq. (6) directly using a sparse linear system solver, e.g. provided by the Eigen3 library [62].

Velocity and Director Profiles.— To determine the average velocity and director profiles in Fig. 2b,d and Extended Data Fig. 4, the model tissue is divided into an N_x by N_y grid [36]. The velocity along x of the plaquette (i, j) is

$$v_{x,(i,j)} = \frac{\sum_{c,t} h_{(i,j)}\left[\mathbf{r}_c(t)\right] v_{x,c}(t)}{\sum_{c,t} h_{(i,j)}\left[\mathbf{r}_c(t)\right]}, \tag{8}$$

where the sum is over all cells c and times between $t = 10^5$ and $t = 2 \cdot 10^5$ in steps of $\delta t = 500$. $\mathbf{r}_c(t)$ is the geometric centre of the cell c at time t, $v_{x,c}(t)$ is the x component of the velocity of cell c, defined as the average velocity of its non-fixed vertices, and the vertex velocity $\mathbf{v}_i(t) = [\mathbf{r}_i(t) - \mathbf{r}_i(t-\Delta t)]/\Delta t$. Finally, the function $h_{(i,j)}(\mathbf{r})$ takes the value 1 if $\mathbf{r}$ lies within plaquette (i, j), and 0 otherwise.

Similarly, the $\mathbf{Q}$ tensor of the plaquette (i, j) is

$$\mathbf{Q}_{(i,j)} = \frac{\sum_{c,t} h_{(i,j)}\left[\mathbf{r}_c(t)\right] \mathbf{Q}_c(t)}{\sum_{c,t} h_{(i,j)}\left[\mathbf{r}_c(t)\right]}, \tag{9}$$

with $\mathbf{Q}_c(t)$ being the $\mathbf{Q}$ tensor of cell c at time t. The mean velocities along the channel width in Fig. 3b are obtained in the same way, except that there are now only N_y plaquettes, each representing one row along the channel.

Mean-Squared Displacement and Mean Velocity.— To determine the mean-squared displacements shown in Fig. 2e and used for fitting in Extended Data 3a-c, as well as the mean velocities in Figs. 2f, 3a, and Extended Data Fig. 2, simulations were first run from $t = -10^5$ until $t = 0$ so that flows could emerge. When simulations started from a flowing profile, they first ran with wet dynamics for a 10^5 long interval before $t = -10^5$. We then calculated $\mathrm{MSD}(t) = \frac{1}{N_c}\sum_c |\mathbf{r}_c(t) - \mathbf{r}_c(0)|^2$, with N_c being the total number of cells. Similarly, the mean velocity along x is given as $\bar{v}_x = \frac{1}{tN_c}\sum_c [x_c(t) - x_c(0)]$, where $x_c(t)$ is the x coordinate of the centre of cell c at time t. To determine the threshold activities for flows to start in Extended Data Fig. 2, we set the threshold $|\bar{v}_x|$ as 10^{-5}. For the dry model in Extended Data 3a,d,g, simulations were first allowed to run from $t = -3 \cdot 10^5$ to 0, and then measurements were taken to $t = 3 \cdot 10^5$.

Analysing flows in the dry model.— To determine if unidirectional flows are in general not possible in the dry model, we scanned over activities in the range $\zeta = 0.01 - 0.2$, and using channel widths $N_y = 6$, 8, 14, and 20. While transport can be superdiffusive, unlike the wet case, it is never ballistic: the mean-squared displacement $\sim t^\beta$, with $\beta < 2$ in all cases (Extended Data Fig. 3). This remains true even if one starts with the wet case and changes it to dry dissipation after a flow profile is developed. The superdiffusive transport arises as the result of the no-slip cells at the channel wall anchoring at an angle relative to the wall as seen in Fig. 2a,c, hence allowing for unidirectional flows near the wall.

To further quantify flows in the dry model, we defined the angle θ_c between the velocity of a cell and the x axis aligned with the direction of the channel. $\langle\cos\theta_c\rangle$ averaged over cells and time is $\approx \pm 1$ for unidirectional flows, and ≈ 0 if flows are predominantly chaotic. Alternatively, we can analyse the modified angle $\tilde{\theta}_c$ which is confined to the range $[0, \pi/2]$ so that $\tilde{\theta}_c = 0$ corresponds to the velocity in the direction along the channel, whereas $\tilde{\theta}_c = \pi/2$ corresponds to the velocity perpendicular to the channel. Therefore, for unidirectional flows, $\langle\tilde{\theta}_c\rangle \approx 0$, whereas for a chaotic flow, $\langle\tilde{\theta}_c\rangle \approx \pi/4$. Measurements of θ_c and $\tilde{\theta}_c$ indeed agree with unidirectional flow in the wet case, and with chaotic flow in the dry case (Extended Data Fig. 3).

ACKNOWLEDGMENTS

We wish to thank M. Krajnc for providing the initial version of the vertex model code, and S. Bhattacharyya, S. Caballero-Mancebo, G. Charras, J. Klebs, A. Košmrlj, F. Mori, A. Weber and C. J. Weijer for many helpful discussions. J.R. and J.M.Y. acknowledge support from the UK EPSRC (Award EP/W023849/1). C.K.V.S. and R.S. acknowledge support from the UK EPSRC (Award EP/W023946/1).

[1] P. Friedl and D. Gilmour, Collective cell migration in morphogenesis, regeneration and cancer, Nat. Rev. Mol. Cell Biol. **10**, 445 (2009).

[2] P. Rørth, Collective cell migration, Annu. Rev. Cell Dev. Biol. **25**, 407 (2009).

[3] M. Poujade, E. Grasland-Mongrain, A. Hertzog, J. Jouanneau, P. Chavrier, B. Ladoux, A. Buguin, and P. Silberzan, Collective migration of an epithelial monolayer in response to a model wound, Proc. Natl. Acad. Sci. U.S.A. **104**, 15988 (2007).

[4] T. J. Shaw and P. Martin, Wound repair at a glance, J. Cell Sci. **122**, 3209 (2009).

[5] P. Friedl, P. B. Noble, P. A. Walton, D. W. Laird, P. J. Chauvin, R. J. Tabah, M. Black, and K. S. Zänker, Migration of coordinated cell clusters in mesenchymal and epithelial cancer explants in vitro, Cancer Res. **55**, 4557 (1995).

[6] J. P. Thiery, Epithelial–mesenchymal transitions in tumour progression, Nature Reviews Cancer **2**, 442 (2002).

[7] C. J. Weijer, Collective cell migration in development, J. Cell Sci. **122**, 3215 (2009).

[8] E. Scarpa and R. Mayor, Collective cell migration in development, J. Cell Biol. **212**, 143 (2016).

[9] C. Collinet and T. Lecuit, Programmed and self-organized flow of information during morphogenesis, Nat. Rev. Mol. Cell Biol. **22**, 245 (2021).

[10] X. Trepat, M. R. Wasserman, T. E. Angelini, E. Millet, D. A. Weitz, J. P. Butler, and J. J. Fredberg, Physical forces during collective cell migration, Nat. Phys. **5**, 426 (2009).

[11] D. T. Tambe, C. C. Hardin, T. E. Angelini, K. Rajendran, C. Y. Park, X. Serra-Picamal, E. H. Zhou, M. H. Zaman, J. P. Butler, D. A. Weitz, *et al.*, Collective cell guidance by cooperative intercellular forces, Nat. Mater. **10**, 469 (2011).

[12] O. Chepizhko, C. Giampietro, E. Mastrapasqua, M. Nourazar, M. Ascagni, M. Sugni, U. Fascio, L. Leggio, C. Malinverno, G. Scita, *et al.*, Bursts of activity in collective cell migration, Proc. Natl. Acad. Sci. U.S.A. **113**, 11408 (2016).

[13] T. B. Saw, A. Doostmohammadi, V. Nier, L. Kocgozlu, S. Thampi, Y. Toyama, P. Marcq, C. T. Lim, J. M. Yeomans, and B. Ladoux, Topological defects in epithelia govern cell death and extrusion, Nature **544**, 212 (2017).

[14] T. E. Angelini, E. Hannezo, X. Trepat, M. Marquez, J. J. Fredberg, and D. A. Weitz, Glass-like dynamics of collective cell migration, Proc. Natl. Acad. Sci. U.S.A. **108**, 4714 (2011).

[15] S. Henkes, K. Kostanjevec, J. M. Collinson, R. Sknepnek, and E. Bertin, Dense active matter model of motion patterns in confluent cell monolayers, Nat. Commun. **11**, 1 (2020).

[16] D. Bi, X. Yang, M. C. Marchetti, and M. L. Manning, Motility-driven glass and jamming transitions in biological tissues, Phys. Rev. X **6**, 021011 (2016).

[17] D. L. Barton, S. Henkes, C. J. Weijer, and R. Sknepnek, Active vertex model for cell-resolution description of epithelial tissue mechanics, PLOS Comput. Biol. **13**, e1005569 (2017).

[18] M. Merkel and M. L. Manning, A geometrically controlled rigidity transition in a model for confluent 3d tissues, New J. Phys. **20**, 022002 (2018).

[19] S. Garcia, E. Hannezo, J. Elgeti, J.-F. Joanny, P. Silberzan, and N. S. Gov, Physics of active jamming during collective cellular motion in a monolayer, Proc. Natl. Acad. Sci. U.S.A. **112**, 15314 (2015).

[20] M. Marchetti, J. Joanny, S. Ramaswamy, T. Liverpool, J. Prost, M. Rao, and R. A. Simha, Hydrodynamics of soft active matter, Rev. Mod. Phys. **85**, 1143 (2013).

[21] A. Doostmohammadi, J. Ignés-Mullol, J. M. Yeomans, and F. Sagués, Active nematics, Nat. Commun. **9**, 1 (2018).

[22] G. Gompper, R. G. Winkler, T. Speck, A. Solon, C. Nardini, F. Peruani, H. Löwen, R. Golestanian, U. B. Kaupp, L. Alvarez, *et al.*, The 2020 motile active matter roadmap, J. Phys. Condens. Matter **32**, 193001 (2020).

[23] R. Alert, J. Casademunt, and J.-F. Joanny, Active turbulence, Annu. Rev. Condens. Matter Phys. **13**, 143 (2022).

[24] V. Hakim and P. Silberzan, Collective cell migration: a physics perspective, Rep. Prog. Phys. **80**, 076601 (2017).

[25] B. Ladoux and R.-M. Mège, Mechanobiology of collective cell behaviours, Nat. Rev. Mol. Cell Biol. **18**, 743 (2017).

[26] T. B. Saw, W. Xi, B. Ladoux, and C. T. Lim, Biological tissues as active nematic liquid crystals, Adv. Mater. **30**, 1802579 (2018).

[27] M. T. Butler and J. B. Wallingford, Planar cell polarity in development and disease, Nat. Rev. Mol. Cell Biol. **18**, 375 (2017).

[28] R. Alert and X. Trepat, Physical models of collective cell migration, Annu. Rev. Condens. Matter Phys. **11**, 77 (2020).

[29] G. S. Nájera and C. J. Weijer, Cellular processes driving gastrulation in the avian embryo, Mech. Dev. **163**, 103624 (2020).

[30] K. Dierkes, A. Sumi, J. Solon, and G. Salbreux, Spontaneous oscillations of elastic contractile materials with turnover, Phys. Rev. Lett. **113**, 148102 (2014).

[31] R. J. Tetley, G. B. Blanchard, A. G. Fletcher, R. J. Adams, and B. Sanson, Unipolar distributions of junctional Myosin II identify cell stripe boundaries that drive cell intercalation throughout drosophila axis extension, eLife **5**, e12094 (2016).

[32] N. Noll, M. Mani, I. Heemskerk, S. J. Streichan, and B. I. Shraiman, Active tension network model suggests an exotic mechanical state realized in epithelial tissues, Nat. Phys. **13**, 1221 (2017).

[33] M. F. Staddon, K. E. Cavanaugh, E. M. Munro, M. L. Gardel, and S. Banerjee, Mechanosensitive junction re-

modeling promotes robust epithelial morphogenesis, Biophys. J. **117**, 1739 (2019).
[34] M. Krajnc, T. Stern, and C. Zankoc, Active instability and nonlinear dynamics of cell-cell junctions, Phys. Rev. Lett. **127**, 198103 (2021).
[35] R. Sknepnek, I. Djafer-Cherif, M. Chuai, C. Weijer, and S. Henkes, Generating active t1 transitions through mechanochemical feedback, eLife **12**, e79862 (2023).
[36] S.-Z. Lin, M. Merkel, and J.-F. Rupprecht, Structure and rheology in vertex models under cell-shape-dependent active stresses, Phys. Rev. Lett. **130**, 058202 (2023).
[37] J. Rozman, J. M. Yeomans, and R. Sknepnek, Shape-tension coupling produces nematic order in an epithelium vertex model, Phys. Rev. Lett. **131**, 228301 (2023).
[38] S. Tlili, J. Yin, J.-F. Rupprecht, M. Mendieta-Serrano, G. Weissbart, N. Verma, X. Teng, Y. Toyama, J. Prost, and T. Saunders, Shaping the zebrafish myotome by intertissue friction and active stress, Proc. Natl. Acad. Sci. U.S.A. **116**, 25430 (2019).
[39] S. Tong, R. Sknepnek, and A. Košmrlj, Linear viscoelastic response of the vertex model with internal and external dissipation: Normal modes analysis, Phys. Rev. Research **5**, 013143 (2023).
[40] R. Voituriez, J.-F. Joanny, and J. Prost, Spontaneous flow transition in active polar gels, Europhys. Lett. **70**, 404 (2005).
[41] M. Saadaoui, D. Rocancourt, J. Roussel, F. Corson, and J. Gros, A tensile ring drives tissue flows to shape the gastrulating amniote embryo, Science **367**, 453 (2020).
[42] M. Serra, G. S. Nájera, M. Chuai, V. Spandan, C. J. Weijer, and L. Mahadevan, Reconstruction of distinct vertebrate gastrulation modes via modulation of key cell behaviors in the chick embryo, Sci. Adv. **9**, abn5429 (2023).
[43] G. Duclos, C. Blanch-Mercader, V. Yashunsky, G. Salbreux, J.-F. Joanny, J. Prost, and P. Silberzan, Spontaneous shear flow in confined cellular nematics, Nat. Phys. **14**, 728 (2018).
[44] S. R. K. Vedula, M. C. Leong, T. L. Lai, P. Hersen, A. J. Kabla, C. T. Lim, and B. Ladoux, Emerging modes of collective cell migration induced by geometrical constraints, Proc. Natl. Acad. Sci. U.S.A. **109**, 12974 (2012).
[45] V. Petrolli, M. Le Goff, M. Tadrous, K. Martens, C. Allier, O. Mandula, L. Hervé, S. Henkes, R. Sknepnek, T. Boudou, *et al.*, Confinement-induced transition between wavelike collective cell migration modes, Phys. Rev. Lett. **122**, 168101 (2019).
[46] R. Farhadifar, J.-C. Röper, B. Aigouy, S. Eaton, and F. Jülicher, The influence of cell mechanics, cell-cell interactions, and proliferation on epithelial packing, Curr. Biol. **17**, 2095 (2007).
[47] R. A. Simha and S. Ramaswamy, Hydrodynamic fluctuations and instabilities in ordered suspensions of self-propelled particles, Phys. Rev. Lett. **89**, 058101 (2002).
[48] S.-Z. Lin, M. Merkel, and J.-F. Rupprecht, Implementation of cellular bulk stresses in vertex models of biological tissues, Eur. Phys. J. E **45**, 1 (2022).
[49] S. P. Thampi, Channel confined active nematics, Curr. Opin. Colloid Interface Sci. **61**, 101613 (2022).
[50] D. Frenkel and B. Smit, *Understanding Molecular Simulation: From Algorithms to Applications*, 2nd ed. (Academic Press, San Diego, 2002).
[51] J. B. Wallingford, S. E. Fraser, and R. M. Harland, Convergent extension: the molecular control of polarized cell movement during embryonic development, Dev. Cell **2**, 695 (2002).
[52] F. Mori, S. Bhattacharyya, J. M. Yeomans, and S. P. Thampi, Viscoelastic confinement induces periodic flow reversals in active nematics, arXiv preprint arXiv:2307.14919 (2023).
[53] M. Chiang, A. Hopkins, B. Loewe, M. C. Marchetti, and D. Marenduzzo, Intercellular friction and motility drive orientational order in cell monolayers, arXiv preprint arXiv:2310.20465 (2023).
[54] B. Li and S. X. Sun, Coherent motions in confluent cell monolayer sheets, Biophys. J. **107**, 1532 (2014).
[55] S. Koride, A. J. Loza, and S. X. Sun, Epithelial vertex models with active biochemical regulation of contractility can explain organized collective cell motility, APL Bioeng. **2** (2018).
[56] S.-Z. Lin, D. Bi, B. Li, and X.-Q. Feng, Dynamic instability and migration modes of collective cells in channels, J. R. Soc. Interface **16**, 20190258 (2019).
[57] C. Fu, F. Dilasser, S.-Z. Lin, M. Karnat, A. Arora, H. Rajendiran, H. T. Ong, N. M. Hoon, S. W. Phow, T. Hirashima, *et al.*, E-cadherin-dependent phosphorylation of egfr governs a homeostatic feedback loop controlling intercellular junction viscosity and collective migration modes., bioRxiv , 2023 (2023).
[58] K. Sato, T. Hiraiwa, and T. Shibata, Cell chirality induces collective cell migration in epithelial sheets, Phys. Rev. Lett. **115**, 188102 (2015).
[59] S. Okuda, E. Kuranaga, and K. Sato, Apical junctional fluctuations lead to cell flow while maintaining epithelial integrity, Biophys. J. **116**, 1159 (2019).
[60] J. Eckert, B. Ladoux, R.-M. Mège, L. Giomi, and T. Schmidt, Hexanematic crossover in epithelial monolayers depends on cell adhesion and cell density, Nat. Commun. **14**, 5762 (2023).
[61] J.-M. Armengol-Collado, L. N. Carenza, J. Eckert, D. Krommydas, and L. Giomi, Epithelia are multiscale active liquid crystals, Nat. Phys. (2023).
[62] G. Guennebaud, B. Jacob, *et al.*, Eigen v3, http://eigen.tuxfamily.org (2010).

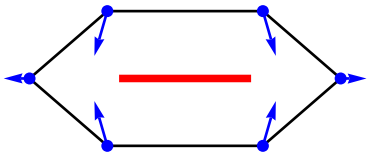

EXTENDED DATA FIG. 1. **Schematic of the active forces**. Blue arrows show active forces on the vertices of an elongated cell arising from the cell's stress tensor. Red line shows the director.

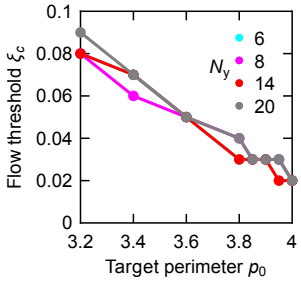

EXTENDED DATA FIG. 2. **Threshold activities decrease with increasing target perimeter**. Threshold activity for unidirectional flows (Methods) for different target perimeters p_0 and channel widths.

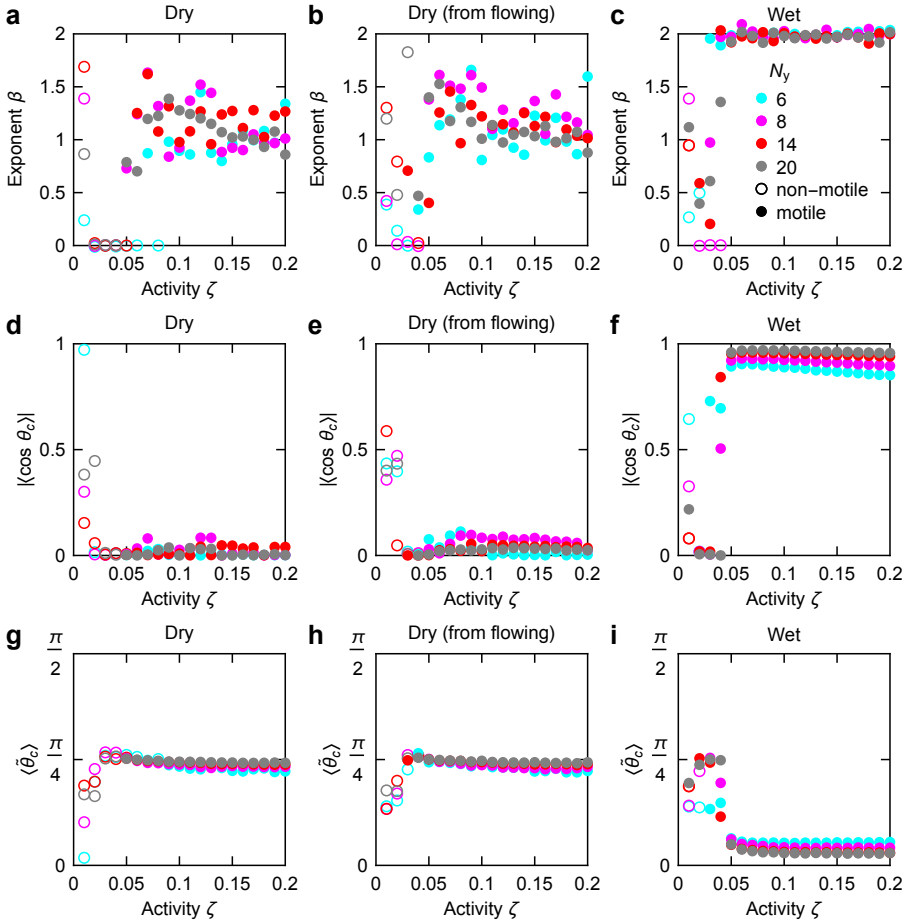

EXTENDED DATA FIG. 3. **Comparing the dry and wet models**. **a-c**) Exponent of αt^{β} fit to MSD for the dry model (**a**), dry model from initial flowing profile (**b**), and wet model (**c**). Legend in panel **c** applies to the entire figure. **d-f**) Absolute value of the average cosine of the angle θ_c between cell velocity and the x axis; average is over all cells and over simulation snapshots between t_1 and t_2 in steps $\Delta t = 500$, for the dry model (**d**; $t_1 = 3 \cdot 10^5$, $t_2 = 6 \cdot 10^5$), dry model from initial flowing profile (**e**; $t_1 = 2 \cdot 10^5$, $t_2 = 3 \cdot 10^5$), and wet model (**f**; $t_1 = 1 \cdot 10^5$, $t_2 = 2 \cdot 10^5$). **g-i**) Average of angle $\tilde{\theta}_c$ (θ confined to the range $[0, \pi/2]$) for the dry model (**g**), dry model from initial flowing profile (**h**), and wet model (**i**); averaging as in corresponding panels **d-f**. Empty circles on all panels correspond to simulations where MSD < 0.1.

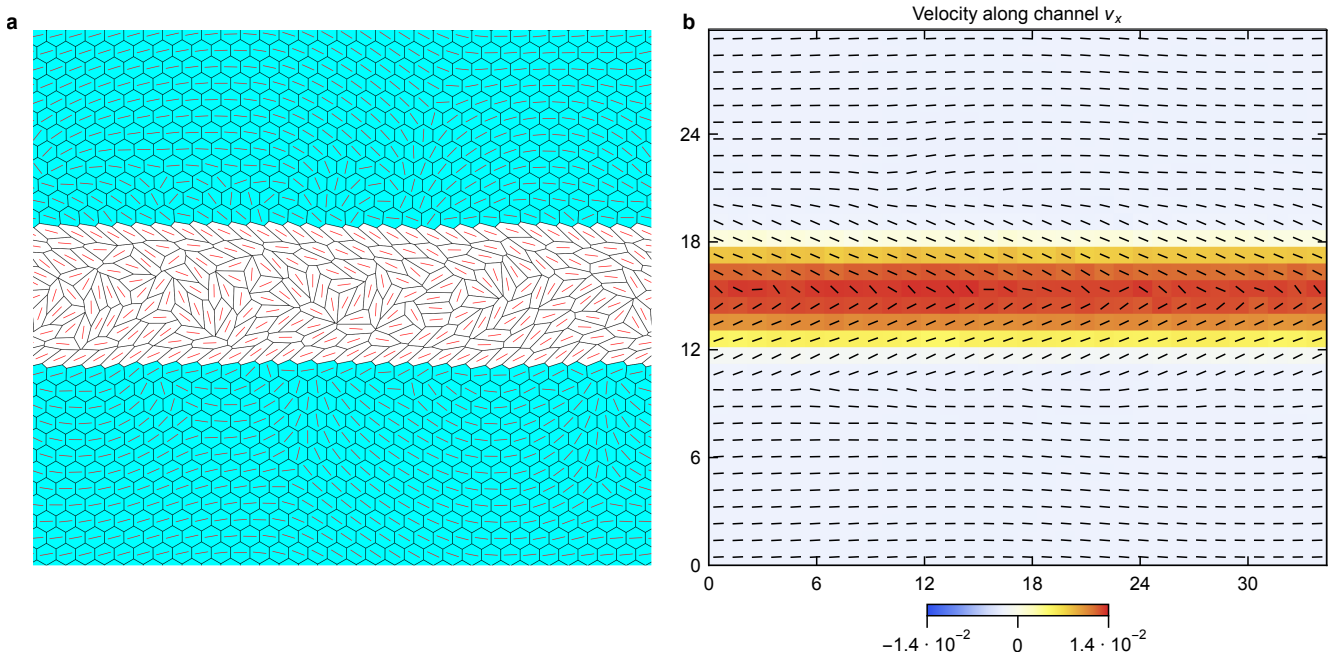

EXTENDED DATA FIG. 4. **Channel flows in a tissue**. **a**&**b**) Model tissue with periodic boundary conditions shown at $t = 2 \cdot 10^5$ (**a**) with the corresponding velocity and director profiles averaged between $t = 1 \cdot 10^5$ and $t = 2 \cdot 10^5$ in increments of $\Delta t = 500$ (**b**). Softer, active white cells have $p_0 = 3.85$ and $\zeta = 0.1$. Solid, passive cyan cells have $p_0 = 1$ and $\zeta = 0$. Red lines show cell directors in **a**, black lines show averaged cell directors in **b**.